1     **Revision 1**

2

3     **First-Principles Prediction of Pressure Enhanced Defect Segregation and Migration at**

4     **MgO Grain Boundaries**

5     **BIJAYA B. KARKI[1,*], DIPTA B. GHOSH[1] AND ASHOK K. VERMA[2]**

6     [1]School of Electrical Engineering and Computer Science, Department of Geology and

7     Geophysics, Center for Computation and Technology, Louisiana State University, Baton Rouge,

8     LA 70803, U.S.A

9     [2]High Pressure Physics Division, Bhabha Atomic Research Center, Mumbai 400085, India

10

11

12                                              **ABSTRACT**

13    Understanding the ability of grain boundaries to accommodate point defects and enhance

14    diffusion rates in mantle materials represents an important but challenging problem. Extant

15    experimental studies and recent computational efforts are mainly limited to the ambient pressure.

16    Here, we investigate this problem for MgO at the atomistic level by performing density

17    functional theory-based simulations of the {310)}/[001] tilt grain boundary in MgO at pressures

18    up to 100 GPa. Our results show that native defects and impurities (Ca, Al, and proton modeled

19    here) favorably segregate to the boundary, with the segregation considerably increasing with

20    pressure. They also imply that grain boundary diffusion is easier, and more anisotropic and

21    complex than bulk (lattice) diffusion: The calculated migration enthalpies for host ions and

22    impurities at the grain boundary are smaller than the bulk values, more so at higher pressures

23    with their values being as low as ~ 1.5 eV at 100 GPa compared to the bulk values of ~ 4 eV.

24    Thus demonstrated high defect activity of grain boundaries in MgO - a major phase of Earth's

25    lower mantle is expected to be relevant to our understanding of mantle rheology and

26    geochemical process.

27

1

28    **Keywords:**  Grain boundaries, defects and diffusion, high pressure, first-principles computation,

29    MgO, and mantle materials

30

2

31 **INTRODUCTION**

32     Grain boundaries (GBs), which exist in most naturally occurring as well as synthesized

33 materials, are known to dramatically influence many physical properties of these materials. GBs

34 are considered to serve as effective sinks for point defects including impurities thereby

35 controlling chemical diffusion, electrical conduction, and creep process, and also as nucleation

36 sites for corrosion, precipitation, fracture, and plastic deformation (Duffy 1986; Sutton and

37 Balluffi 1995; Hiraga et al. 2004; Dohmen and Milke 2010). These effects can be considered to

38 arise mainly because the interfacial regions separating the component crystal grains contain

39 structural distortions and void spaces (e.g., Kingery 1974; Duffy 1986; McKenna and Shluger

40 2009; Wang et al. 2011). Such interfacial features are likely to be highly sensitive to pressure as

41 suggested by some calculations (Harris et al. 1999; Verma and Karki 2010). Much less is,

42 however, known about the way pressure controls the ability of GBs to accommodate native and

43 impurity defects, and influence diffusion rates.

44     Here, we investigate the effects of pressure on the interplay between point defects and GBs in

45 materials by considering MgO - a prototype metal-oxide and a technologically important

46 ceramic. Moreover, (Mg,Fe)O – thought to be the second most abundant mineral in the Earth's

47 lower mantle, which is essentially a polycrystalline rock subject to high pressure up to 136 GPa,

48 and to that end, the knowledge about grain boundary properties can have profound

49 geophysical/geochemical implications. In particular, the importance of grain boundaries for

50 understanding of chemical distribution in the mantle has been widely discussed (e.g., Hiraga et

51 al. 2004; Hayden and Watson 2007; Dohmen and Milke 2010). Extant experimental

52 measurements are limited to the ambient or low pressures. The tilt boundaries in MgO were

53 observed as atomic resolution images (e.g., Yan et al. 1998; Wang et al. 2011). Fast diffusion was

54 measured for cations and oxygen, and siderophile elements in polycrystalline MgO (Oishi and

55 Kingery 1960; Wuensch and Vasilos 1966; Hashimoto and Hama 1971; Chang et al. 1981;

56 Kizuka et al. 1998; Hayden and Watson 2007). To extend our understanding of the GBs to high-

57 pressure regime, we perform the density-functional theory-based computation, which is widely

58 accepted to make accurate prediction at the macroscopic (bulk) level as well as allow access to

59 atomistic information. Previous studies were mostly based on pair potentials, which allow fast

3

60   computation but have a disadvantage of being empirical (e.g., Harris et al. 1999; Browning et al.

61   1999; Karki and Kumar 2007; Adjaoud et al. 2012).

62       The first principles approach has so far been applied to tilt grain boundaries in materials with

63   focus on their atomic and electronic structures (Yan et al. 1998; McKenna and Shluger 2008;

64   2009; Ghosh and Karki 2014). We have previously simulated $\{n10\}/[001]$ tilt boundaries in

65   MgO to show that the boundary structures vary considerably with pressure and also show that

66   vacancy defects favorably segregate to the boundaries (Verma and Karki 2010). Here, we extend

67   our simulations to the incorporation and migration of impurities including Ca, Al, and proton at

68   MgO tilt boundaries as a function of pressure. These defects are likely to be present in MgO

69   under most environments including those of the Earth's interior. The issues we aim to address

70   here are whether these defects segregate to grain boundaries from the bulk, and if they do, how

71   these defects migrate through the boundary region over wide pressure regime.

72

73                                    **METHODOLOGY**

74       Computations were performed using the local density approximation and projector-

75   augmented-wave method as implemented in VASP software (Kresse and Furthmuller 1996). A

76   plane wave basis set with the cut-off of 450 eV was used to expand the valence electron wave

77   functions at $\Gamma$ point.  The Pulay correction of 1 to 2 GPa over the pressure regime (0 to 100 GPa)

78   studied was applied. The fully optimized configurations for the $\{n10\}/[001]$ tilt grain boundaries

79   ($n = 2$, 3 and 4) in MgO from our previous first-principles simulations (Verma and Karki 2010)

80   were used with the main focus on $\sum 5$ (310)/[001] (tilt angle of 36.8º) boundaries. The simulated

81   symmetric tilt GB stable at the zero pressure can be viewed as a series of dislocation pipes

82   forming a well-defined channel structure. Such open structure is less pronounced and becomes

83   denser in the asymmetric tilt GBs (in which the grains have shifted relative to each other along

84   the boundary plane) stable at 50 and 100 GPa (Verma and Karki 2010). Pressure thus suppresses

85   the excess volume, thereby affecting the type of coordination defects and the degree of bond

86   distortions at the interface. Further details on the input configuration, structural relaxation, and

87   point defects can be found in Verma and Karki (2010). For instance, we extract an Mg ion

88   leaving two valence electrons to create a cationic vacancy ($V''_{Mg}$) whereas we replace Mg ion

89   with a different cation of the same or different charge to create an impurity defect. Atomic

4

90    positions were relaxed at fixed cell parameters so pressure was imposed by a constant volume

91    approach. The defect-defect coulomb interactions, arising due to periodic boundary conditions,

92    were treated as earlier (Karki and Khanduja 2006; Verma and Karki 2010). The supercells

93    contained 560 atoms for both types (symmetric and asymmetric) of grain boundaries studied.

94    Doubling the supercell did not affect the calculated results significantly.

95

96                               **RESULTS AND DISCUSSION**

97    **Grain boundary segregation of defects**

98          Unlike the bulk region, the interfacial region contains many nonequivalent sites and void

99    regions where defects can reside. Only Mg sites labeled *A, B, C* and *D* at the MgO {310}/[001]

100   tilt boundary region and interstitial sites which are at (or closest to) the boundary plane were

101   considered (Fig. 1). We have previously calculated the energetics and structures of Mg and O

102   vacancies at these boundary sites as a function of pressure and shown that both cation and anion

103   vacancies favorably segregate to the grain boundaries of MgO (Verma and Karki 2010). Here, we

104   characterize the tendency of impurities (Ca, Al and proton) to segregate to GBs by considering

105   substitution and interstitial mechanisms. For this purpose, we simulate a given defect one time in

106   the bulk region and the other time in the grain boundary region, and compare the formation

107   energies between the two cases. The segregation enthalpy of the concerned defect from the bulk

108   can be calculated as: $\Delta H_S = H_{GB} - H_{Bulk}$, where $H_{GB}$ and $H_{Bulk}$ are the enthalpies of the supercells

109   containing the defect in the boundary and bulk regions, respectively. A negative value of $\Delta H_S$

110   means that the grain boundary site is energetically more favorable than the bulk site – the

111   corresponding defects from the bulk segregate to the grain boundary.  Note that $\Delta H_S$ is

112   independent of both atomic and electronic chemical potentials. Also, for a charged defect, the

113   defect-defect corrections cancel out since the same correction (and band alignment) applies to

114   the both cases of the supercell: one with the defect at the bulk site and the other with the defect at

115   the boundary site (Karki and Khanduja 2006).

116         We find that all four $Ca_{Mg}^{\times}$ configurations at the boundary have lower enthalpies than at the

117   bulk site with the site *B* being the most stable (by 0.9 eV) for the symmetric GB at zero pressure

118   (Table 1). The Ca substitution forms octahedral coordination at *B* unlike other three under-

5

119  coordinated sites (Fig. 1), and also each local structure is much more relaxed compared to bulk

120  site. The Ca segregation to particular atomic columns in the GB was experimentally observed at

121  the ambient pressure (Yan et al. 1998). Not all boundary sites are energetically favorable in

122  asymmetric GBs (Table 1); the sites *A* and *C* being the most and least stable, respectively. The Ca

123  segregation enthalpy increases with pressure by a factor of two reaching 2.1 eV at 100 GPa.

124  Similarly, the segregation enthalpy of $Al^{\bullet}_{Mg}$ (trivalent cation substituting Mg) was shown to

125  increase with pressure (0.2 to 0.5 eV between 0 and 100 GPa). The sites *A* and *D* are stable for

126  the symmetric boundary whereas only the site *C* is stable for the asymmetric boundaries at zero

127  and elevated pressures (Table 1). For proton defects, we show that the substitution is more

128  favorable at the boundary sites than at the bulk site with double proton preferred over single

129  proton. When two protons occupy a vacant Mg site, a $2H^{\times}_{Mg}$ defect is created. At zero pressure,

130  the boundary site *B* is preferred most with segregation enathlpy of -1.14 eV, which increases to -

131  2.63 eV at 100 GPa (Table 1).

132      We consider possible interstitials in the open space of the boundary versus the interstitial

133  bulk sites for $Ca^{\bullet\bullet}_i$ and $Al^{\bullet\bullet\bullet}_i$ as well as host cation ($Mg^{\bullet\bullet}_i$). The GB interstitials were found to be

134  distinctly preferred by each cation type over the bulk interstitials by several eVs (> 5 eV) at all

135  pressures, indicating strong segregation to the boundary. This tendency can be attributed to the

136  ion size mis-fit effect because the interstitial cations can easily fit in the excess free space of the

137  boundary and also the boundary atoms can undergo large relaxations. The impurities behave as

138  somewhat delocalized defects in the central part of the GB void space in both symmetric and

139  asymmetric boundaries though the sites are more constricted at the elevated pressures.

140      For interstitial proton ($H^{\bullet}_i$ or $p_i$), we have located three inequivalent adsorption sites in the

141  symmetric GB open space at zero pressure, each involving binding of the proton to O (forming a

142  hydroxyl). These sites are energetically more favorable than the bulk site by up to 1.5 eV,

143  consistent with previous calculations (McKenna and Shluger, 2009). The boundary segregation

144  enthalpy of interstitial proton is -2.7 and -2.3 eV at 50 and 100 GPa, respectively (Table 1). At

145  the mid pressure, proton bridges two oxygen ions ($B_L$ and $B_R$ sites, Fig. 1) from two grains to

146  form a strongly bound state. An interstitial proton induces an unoccupied electronic state below

147  the conduction band and can trap an electron to form H atom, whose segregation enthalpy

148  increases from -1.2 eV at 0 GPa to -2.5 eV at 100 GPa.

6

149

## Defects migration at grain boundary

150

151     To study ionic self-diffusion at grain boundaries, we locate saddle points and possible

152     pathways for migration of host ions and impurities by trying a series of positions. For each

153     position, the migrating ion was allowed to have a perpendicular movement and the rest of the

154     super-cell was allowed to relax around it as in previous studies (Harris et al. 1997; Verma and

155     Karki 2009). Also, the migration energy for a charged defect is not influenced by the defect-

156     defect corrections (Karki and Khanduja 2006). The (310)/[001] tilt boundary involves two types

157     of diffusion pathways, one is *along* the boundary (the perpendicular direction to the tilt axis) and

158     the other is *down* the boundary (the direction of the tilt axis). These two directions are

159     represented by the *y*- and *z*-axes, respectively (Fig. 1 and 2), and note that two grains in the

160     simulated bi-crystal system are rotated about the *z*-axis (the tilt axis). Ionic diffusion along the

161     boundary involves migration between the open channels whereas the diffusion down the

162     boundary is confined within single GB core.

163     The directions of migration (via vacancy hopping) and associated activation enthalpies for

164     the host ions ($Mg^{2+}$ and $O^{2-}$) in the symmetric (0 GPa) and asymmetric (100 GPa) tilt boundaries

165     are shown in Figure 2. The calculated migration enthalpy varies considerably for jumps between

166     consecutive sites, and the trend is similar between the cation and anion (Table 2). The vacancy

167     hopping along the boundary (*y*-direction) occurs from one dislocation pipe to an adjacent one so

168     migrating ion remains on the same grain. The activation energies for most steps are lower than

169     the bulk migration enthalpies, and the diffusion-rate determining step occurs between the sites *C*

170     and *D* with activation enthalpies of 2.3 eV (cation) and 2.2 eV (anion) for the {310} symmetric

171     boundary. For migration down the boundary (*z*-direction), the most favorable step occurs

172     between the opposite faces of the boundary via $A_L$ and $A_R$ sites with activation energies of 1.5 eV

173     (cation) and 1.3 eV (anion). Other energetically competitive path involves hopping between *B*

174     and *C* sites with migrating ion remaining on the same grain.  The calculated migration enthalpies

175     for the {210} and {410} symmetric tilt grain boundaries at zero pressure are similar to the values

176     for the {310} boundary (Table 2).

177     We find that pressure affects the boundary diffusion in a more complicated way than the bulk

178     ionic diffusion (Ita and Cohen 1997; Harris et al. 2001; Van Orman et al. 2003; Karki and

7

179    Khanduja 2006). The predicted enthalpies for diffusion along the boundary strongly increase

180    with pressure and remain comparable with the corresponding bulk values (Table 2, Fig. 2).

181    However, their values for diffusion down the boundary at 50 and 100 GPa are slightly smaller

182    and larger, respectively, than those at the zero pressure (Table 2). The paths between $B_L$ to $B_R$

183    constitute the most favorable pathway downward with the migration enthalpies (of 1.2 to 1.7 eV

184    at high pressures) being smaller by a factor of 2 to 3 compared to the bulk values (Fig. 2). It is

185    remarkable that the predicted grain boundary diffusion in MgO is highly anisotropic with much

186    faster migration down the boundary whereas the bulk (lattice) diffusion is isotropic.

187    We now discuss the migration of three cations ($Mg_i^{2+}$, $Ca_i^{2+}$ and $Al_i^{3+}$) via interstitials in the

188    boundary region. At zero pressure, an impurity ion migrates down the boundary (*z*-direction) by

189    always remaining close to the center of the GB void space (Fig. 3, S1). The energy barriers are

190    small: 0.4 eV for Mg, 0.2 eV for Ca, and 0.7 eV for Al (Table 3) so these cations can easily

191    migrate down the boundary, and can cover large distances as shown by our direct first-principles

192    molecular dynamics simulations at 1000 K (S2 and S3). The impurity cation also shifts in the *x-y*

193    plane away from the center of void space at elevated pressures (Fig. 3). The diffusion of impurity

194    cation along the boundary also requires a cooperative process involving migration of host cation.

195    The migrating cation may eventually knock out Mg ion from one of two closest $A_L$ and $A_R$ sites

196    (Fig. 3, S1). The maximum barrier occurs just after the migrating cation crosses the $B_L$-$B_R$ plane,

197    and the barrier height and location differ somewhat among three cationic types.

198    At high pressures, the migration has to cover dense (congested) regions separating two

199    successive void spaces and requires interstitial transitions involving more ions. At 100 GPa, the

200    cation passes through the $B_L$-$B_R$ plane by pushing the nearest host cations away, and then passes

201    via one side (left or right) of site *A* (Fig. 3). It may eventually knock out Mg ion from at *D* to the

202    void space. This knocking out process occurs in two steps at 100 GPa (S4). The diffusion down

203    the boundary is essentially confined in the void region and may not require any such transition.

204    These differences make the cationic diffusion at the grain boundary highly anisotropic with the

205    activation enthalpies for migration along the boundary being larger than those for migration

206    down the boundary at all pressures (Table 3).

207    In the boundary region, a migrating proton tends to always remain close to O ion thereby

208    switching from one O-H bonding state to other (i.e., hopping between O ions). When the proton

8

209    migrates down the boundary (*z*-direction), it follows two energetically competitive paths at zero

210    pressure, with the saddle point lying at the boundary plane, as shown in Figure 4. One path is

211    bulged towards the $B_L$-$B_R$ line (in the *y*-direction) with the saddle point lying at the intersection

212    of this line with the boundary plane. The other path is bulged in the opposite direction (i.e.,

213    towards the $A_L$-$A_R$ line). In either case, the migrating proton switches side (from left to right or

214    vice versa). On the other hand, while migrating along the boundary (*y*-direction), the proton

215    remains bound to O ions on the same side. The saddle point lies at the $A_L$-$A_R$ line. The calculated

216    activation enthalpies for proton migration *along* and *down* the boundary are comparable (1.0 to

217    1.2 eV) at zero pressure (Table 3). The effects of pressure on proton migration are non-

218    monotonic: The migration enthalpies for both pathways at 50 GPa are larger than those at zero

219    pressure and 100 GPa. This can be associated with more strongly bound proton site at the mid

220    pressure as pointed out earlier. It is important to note that the boundary saddle point energies at

221    all pressures are always lower than any bulk interstitial and saddle point energies. This means

222    that proton migration should remain confined in the grain boundary region.

223

## IMPLICATIONS

225    Many defects of both native and impurity types in multiple charge states other than those

226    considered here are possible. This is more so in MgO because of its existence in the Earth's

227    mantle, which is thought to contain many other elements including Fe, C, S, Cr, Na, K, Si, etc. in

228    varying amounts. To maintain overall charge neutrality, defects of opposite charges must be

229    present. For instance, two substituted Al ions require one charge-compensating Mg vacancy. If

230    Al impurity exists as GB interstitial, 3 vacancies are formed for two Al ions. Thus, boundary

231    interstitial cations can induce more vacancies, preferably, at boundary sites, perhaps forming

232    bound defect complexes. Al impurity and Mg vacancies can form stable $2Al^{\bullet}_{Mg} + V''_{Mg}$

233    configuration (Ammann et al. 2012) that we have also found to favor the boundary over the bulk.

234    It is important to note that impurity-controlled defects are of extrinsic origin (i.e., they are not

235    thermally produced). Our calculated migration enthalpies thus represent effective activation

236    enthalpies ($E_A$'s) for extrinsic diffusion, which can be used in the Arrhenius equation for the

237    diffusion coefficient: $D = D_0 \exp[-E_A / RT]$ (where $D_0$, $R$ and $T$ are the pre-exponential

238    diffusion coefficient, gas constant and temperature, respectively) to make some quantitative

9

239  comparison between the grain boundary and bulk diffusion contributions. Considering $E_A$'s of

240  ~1.5 eV for migration down the boundary (and assuming the same pre-exponential factors for the

241  boundary and bulk diffusion), we predict GB diffusion rates ($D_{GB}$) to be several orders ($10^4$ to

242  $10^6$) magnitudes higher than the bulk (lattice) diffusion rates ($D_L$).  Our predicted $D_{GB}/D_L$ ratios

243  are comparable with those estimated for dominant grain boundary diffusion of different ions for

244  grain size of 1 cm or smaller expected in mantle minerals (Dohman and Mike 2010).

245  Our first-principles calculations suggest that not only vacancy defects but also impurities

246  readily segregate to the boundary, and pressure increasingly stabilizes all types of defects at the

247  boundaries, i.e., enhances segregation effects. Moreover, pressure enhancement of the ion

248  mobility at the boundary region relative to the bulk (lattice) becomes more effective at higher

249  pressures. The predicted high defect activity can be considered to arise from the electrostatic and

250  elastic forces present at the boundary region increasing with pressure. Our results can have

251  profound implications for the lower mantle because (Mg,Fe)O is considered to be the second

252  most abundant material of this region. First, the predicted large segregation effects and low

253  activation migration enthalpies imply that the grain boundaries could be regions of primary

254  storage for point defects (impurities) in mantle rocks, consistent with suggestions based on low-

255  pressure experimental observations of large segregation of incompatible elements, in particular,

256  (Yan et al. 1998; Hiraga and Kohlstedt 2007). Also, the ionic transport in the deep mantle

257  mediated by grain boundary diffusion could cover long distances (several kilometers) over the

258  geological time scales thereby controlling geochemical processes via elemental redistribution

259  and fractionation (Hiraga et al. 2007; Hayden and Watson 2007). Second, enhanced ionic

260  diffusion could facilitate creep process, which is thought to drive mantle convection (Poirier

261  1985). To further assess these implications, we anticipate further study of more grain boundaries

262  and their effects on point defects in other key mantle minerals. Also important is to study the

263  effects of temperature on the boundary structures, and the boundary incorporation and migration

264  of defects, which we anticipate to simulate using the first-principles molecular dynamics method.

265

10

# REFERENCES CITED

271
272
273 Adjaoud, O., Marquardt, K., and Jahn, S. (2012) Atomic structures and energies of grain
274     boundaries in $Mg_2SiO_4$ forsterite from atomistic modeling. Physics and Chemistry of
275     Minerals, 39, 749–760.

276 Ammann, M.W., Brodholt, J.P., and Dobson, D.P. (2012) Diffusion of aluminum in MgO from
277     first principles. Physics and Chemistry of Minerals, 39, 503–514.

278 Browning, N.D., Buban, J.P., Moltaji, H.O., and Duscher, G. (1999) Investigating the structure-
279     property relationships at grain boundaries in MgO using bond-valence pair potentials and
280     multiple scattering analysis. Journal of American Ceramic Society, 82, 366–372.

281 Chang, Y.M., Henriksen, A. F., and Kingery, W.D., 1981. Characterization of grain boundary
282     segregation in MgO. J. Am. Ceram. Soc. 64, 385 – 389.

283 Dohmen, R., and Milke, R., (2010) Diffusion in polycrystalline materials: Grain boundaries,
284     mathematical models, and experimental data. In: Diffusion in Minerals and Melts. Reviews
285     of Mineralogy and Geochemistry, 72, 921–970.

286 Duffy, D.M. (1986) Grain boundaries in ionic crystals. Journal of Physics C: Solid State Physics,
287     19, 4393–4412.

288 Ghosh, D.B., and Karki, B.B. (2014) First principles simulations of the stability and structure of
289     grain boundaries in $Mg_2SiO_4$ forsterite, Physics and Chemistry of Minerals, 41, 163–171.

290 Harris, D.J., Watson, G.W., and Parker, S.C. (1997) Vacancy migration at the {410}/[001]
291     symmetric tilt grain boundary of MgO: An atomistic simulation study. Physical Review B,
292     56, 11477–11484.

293 Harris, D.J., Watson, G.W., and Parker, S.C. (1999) Computer simulation of pressure-induced
294     structural transitions in MgO [001] tilt grain boundaries. American Mineralogist, 84, 138–
295     143.

296 Harris, D.J., Watson, G.W., and Parker, S.C. (2001) Atomistic simulation studies on the effect of
297     pressure on diffusion at the MgO {410}/[001] tilt grain boundary. Physical Review B, 64,
298     134101.

299 Hashimoto, H., and Hama, M. (1971) Preferential diffusion of oxygen along grain boundaries in
300     polycrystalline MgO. Journal of Applied Physics, 43, 4828–4829.

301 Hayden, L.A., and Watson, E.B. (2007) A diffusion mechanism for core-mantle interaction.
302     Nature, 450, 709–712.

303 Hiraga, T., Anderson, I.M., and Kohlstedt, D.L. (2004) Grain boundaries as reservoirs of
304     incompatible elements in the Earth's mantle. Nature, 427, 699–703.

305 Hiraga, T., and Kohlstedt, D.L. (2007) Equilibrium interface segregation in the diopside-
306     forsterite system I: Analytical techniques, thermodynamics, and segregation characteristics.
307     Geochima et Cosmochimica Acta, 71, 1266-1280.

308 Hiraga, T., Hirschmann, M.M., and Kohlstedt, D.L. (2007) Equilibrium interface segregation in
309     the diopside-forsterite system II: Applications of interface enrichment to mantle
310     geochemistry. Geochima et Cosmochimica Acta, 71, 1281-1289.

12

311   Ita, J., and Cohen, R.E. (1997) Effects of pressure on diffusion and vacancy formation in MgO
312       from nonempirical free-energy integrations. Physical Review Letters, 79, 3198–3201.

313   Karki, B.B., and Khanduja, G. (2006) Vacancy defects in MgO at high pressure. American
314       Mineralogist, 91, 511–516.

315   Karki, B.B., and Kumar, R. (2007) Computer simulation of grain boundary structures in
316       minerals. Proceedings of ICCES'07, 885–891.

317   Kingery, W.D. (1974) Plausible concepts necessary and sufficient for interpretation of ceramic
318       grain boundary phenomena. I. Grain boundary characteristics, structure, and electrostatic
319       potential. Journal of American Ceramic Society, 57, 18.

320   Kizuka, T., Iijima, M., and Tanaka, N. (1998) Atomic process of electron-irradiation-induced
321       grain boundary migration in MgO tilt boundary. Philosophical Magazine A, 77, 413–422.

322   Kresse, G., and Furthmuller, J. (1996) Efficiency of ab-initio total energy calculations for metals
323       and semiconductors using a plane-wave basis set. Computational Materials Science, 6, 15–
324       50.

325   McKenna, K.P., and Shluger, A. (2008) Electron-trapping polycrystalline materials with negative
326       electron affinity. Nature Materials, 7, 859–872.

327   McKenna, K.P., and Shluger, A. (2009) First-principles calculations of defects near a grain
328       boundary in MgO. Physical Review B, 79, 224116.

329   Oishi, Y., and Kingery, W.D. (1960) Oxygen diffusion in periclase crystals. Journal of Chemical
330       Physics, 33, 905–906.

331   Poirier, J.P. (1985) Creep of Crystals: high-temperature deformation processes in metals,
332       ceramics and minerals. Cambridge University Press, Cambridge.

333   Sutton, A.P., Balluffi, R.W. (1995) Interfaces in Crystalline Materials (Clarendon, Oxford).

334   Van Orman, J.A., Fei, Y., Hauri, E.H., Wang, J. (2003) Diffusion in MgO at high pressures:
335       Constraints on deformation mechanisms and chemical transport at the core-mantle boundary.
336       Geophysical Research Letters, 30, 1056, doi:10.1029/2002GL016343.

337   Verma, A.K., and Karki, B.B. (2009) Ab initio investigation of native and protonic point defects
338       in $Mg_2SiO_4$ polymorphs under high pressure. Earth and Planetary Science Letters, 285, 140–
339       149.

340   Verma, A.K., and Karki, B.B. (2010) First-principles simulations of MgO tilt grain boundary:
341       Structure and vacancy formation at high pressure. American Mineralogist, 95, 1035–1041.

342   Wang, Z., Saito, M., McKenna, K.P., Gu, L., Tuskimoto, S., Shluger, A.L., and Ikuhara, Y. (2011)
343       Atom resolved imaging of ordered defect superstructures at individual grain boundaries.
344       Nature, 479, 380–383.

345   Wuensch, B.J., and Vasilos, T. (1966) Origin of grain boundary diffusion on MgO. Journal of
346       American Ceramic Society, 49, 433-463.

347   Yan, Y., Chisholm, M.F., Duscher, G., Maiti, A., Pennycook, S.J., and Pantelides, S.T. (1998)
348       Impurity induced structural transformation of a MgO grain boundary. Physical Review
349       Letters, 81, 3675–3678.

13

350
351

352 **TABLE 1.** Segregation energies (in eV) for various impurities (Ca, Al, and proton) at different
353 sites (*A, B, C,* and *D* shown in Fig. 1) of the {310} tilt symmetric (0 GPa) and asymmetric (0, 50
354 and 100 GPa) boundaries. All energies are defined with respect to the bulk site of the boundary-
355 bearing supercell. Mg-vacancy segregation energies are shown for comparison.

356

357
358
359

|  | Site | $V''_{Mg}$ | $Ca^{\times}_{Mg}$ | $Al^{\times}_{Mg}$ | $2H^{\times}_{Mg}$ | $p_i$ |
|---|---|---|---|---|---|---|
| {310} sym 0 GPa | A | 0.05 | -0.10 | -0.19 | -1.00 | -1.5 |
|  | B | 0.18 | -0.93 | 0.02 | -1.14 |  |
|  | C | -0.21 | -0.72 | 0.17 | -0.77 |  |
|  | D | 0.73 | -0.05 | -0.13 | -0.64 |  |
| {310} asym 0 GPa | A | 0.13 | -0.03 | 0.01 | -0.79 | -1.5 |
|  | B | -1.30 | 0.19 | 0.31 | -0.46 |  |
|  | C | 0.24 | 0.47 | -0.17 | -0.85 |  |
|  | D | -1.13 | 0.00 | 0.37 | -1.06 |  |
| {310} asym 50 GPa | A | 1.17 | -0.42 | 0.02 | -1.41 | -2.7 |
|  | B | -1.82 | -0.15 | 0.62 | -2.27 |  |
|  | C | 1.16 | 1.52 | -0.37 | -0.90 |  |
|  | D | -1.21 | 0.0 | 0.54 | -2.15 |  |
| {310} asym 100 GPa | A | -1.01 | -2.10 | 0.63 | -1.42 | -2.3 |
|  | B | -2.67 | -1.73 | 0.77 | -2.37 |  |
|  | C | -0.90 | 0.36 | -0.53 | -0.98 |  |
|  | D | -2.50 | -0.54 | 0.16 | -2.63 |  |

384
385

14

386 **TABLE 2**. Activation enthalpies (in eV) for $Mg^{2+}$ and $O^{2-}$ ion migration *along* and *down* the

387 {310}, {210} and {410} symmetric boundaries at 0 GPa and {310} asymmetric boundaries at 50

388 and 100 GPa. The bulk values are from Karki and Khanduja (2006). Previous MD results for the

389 {410} symmetric boundary are from Harris et al. (1997).

390

391

|  | Along boundary | | Down boundary | | Bulk | |
|---|---|---|---|---|---|---|
|  | Mg | O | Mg | O | Mg | O |
| {310}, 0 GPa | 2.1 | 2.2 | 1.5 | 1.3 | 2.6 | 2.4 |
| {210}, 0 GPa | 2.3 | 2.4 | 1.2 | 1.4 | | |
| {410}, 0 GPa | 2.3 (2.3) | 2.2 (2.3) | 1.7 (1.1) | 1.5 (1.0) | | |
| {310}, 50 GPa | 3.1 | 3.9 | 1.2 | 1.2 | 3.2 | 3.5 |
| {310}, 100 GPa | 3.5 | 4.3 | 1.6 | 1.7 | 3.8 | 4.2 |

392

393

394

395

15

396 **TABLE 3.** Activation enthalpies (in eV) for interstitial migration of impurities ($Ca^{2+}$, $Al^{3+}$,

397 and proton) and host cation ($Mg^{2+}$) *along* and *down* the {310} symmetric (0 GPa) and

398 asymmetric (50 and 100 GPa) boundaries.

399

|          | Along boundary | | | | Down boundary | | | |
|----------|-----|-----|-----|-----|-----|-----|-----|-----|
|          | Mg  | Ca  | Al  | H   | Mg  | Ca  | Al  | H   |
| 0 GPa    | 2.6 | 3.0 | 3.2 | 1.2 | 0.4 | 0.2 | 0.7 | 1.0 |
| 50 GPa   | 2.3 | 2.6 | 1.9 | 2.1 | 0.8 | 1.5 | 1.3 | 3.0 |
| 100 GPa  | 2.4 | 2.7 | 2.1 | 1.2 | 1.3 | 1.3 | 1.2 | 1.9 |

16

**FIGURE 1.** Local structures of Ca impurity substituted the boundary and bulk sites at zero pressure (left) and 100 GPa (right) shown as polyhedra. Ca-O bond lengths are compared with Mg-O bond lengths (parenthesis). All boundary sites (*A, B, C* and *D*) are also marked. The green (small) and red (large) spheres represent Mg and O atoms, respectively.
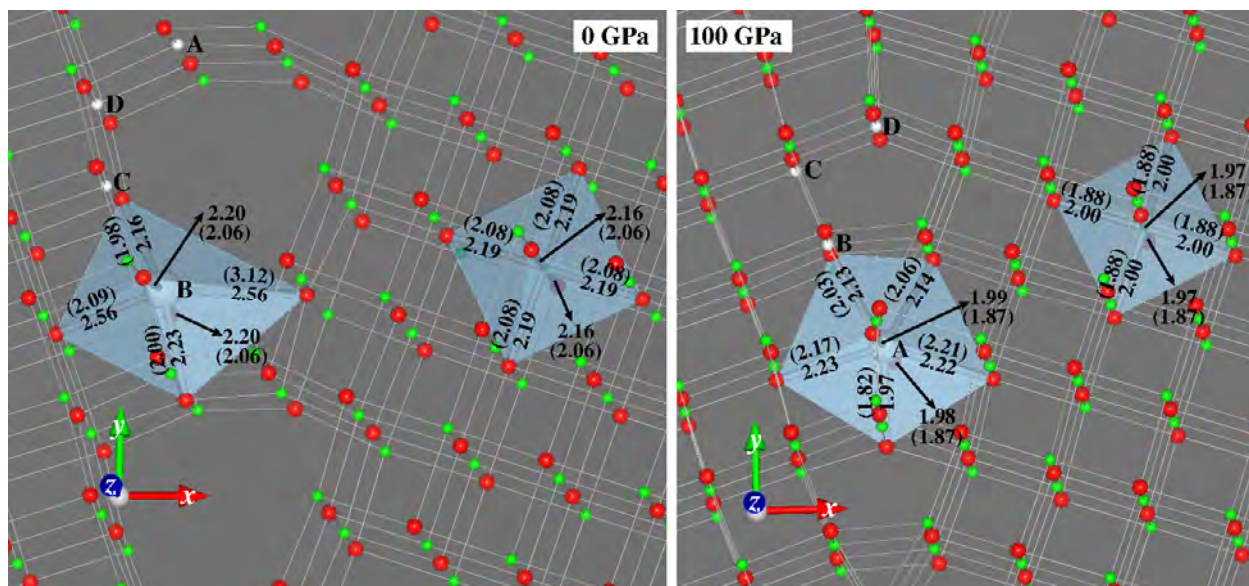
406    **FIGURE 2.** Local migration directions and energies (in eV) for Mg$^{2+}$ ion (first number) and O$^{2-}$
407    ion (second number) in the {310} symmetric boundary at 0 GPa (left) and asymmetric boundary
408    at 100 GPa (right). The green (small) and red (large) spheres represent Mg and O atoms,
409    respectively. The sites are labeled with the subscript L for the left grain and R for the right grain.
410
411
412
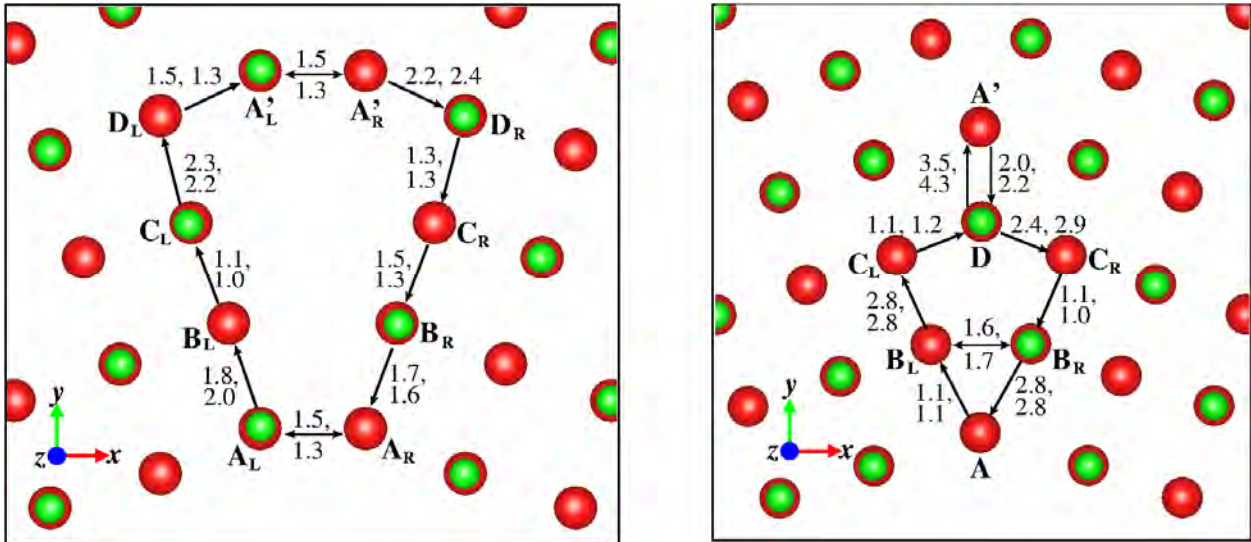


413
414
415
416
417
418
419
420
421
422

18

423    **FIGURE. 3.**  Paths for cation (Mg/Ca/Al) migration at 0 and 100 GPa. The successive positions
424    of the migrating ion are displayed by large sphere with gray color representing the *z*-coordinate.
425    The green (small) and red (large) spheres represent Mg and O, respectively.
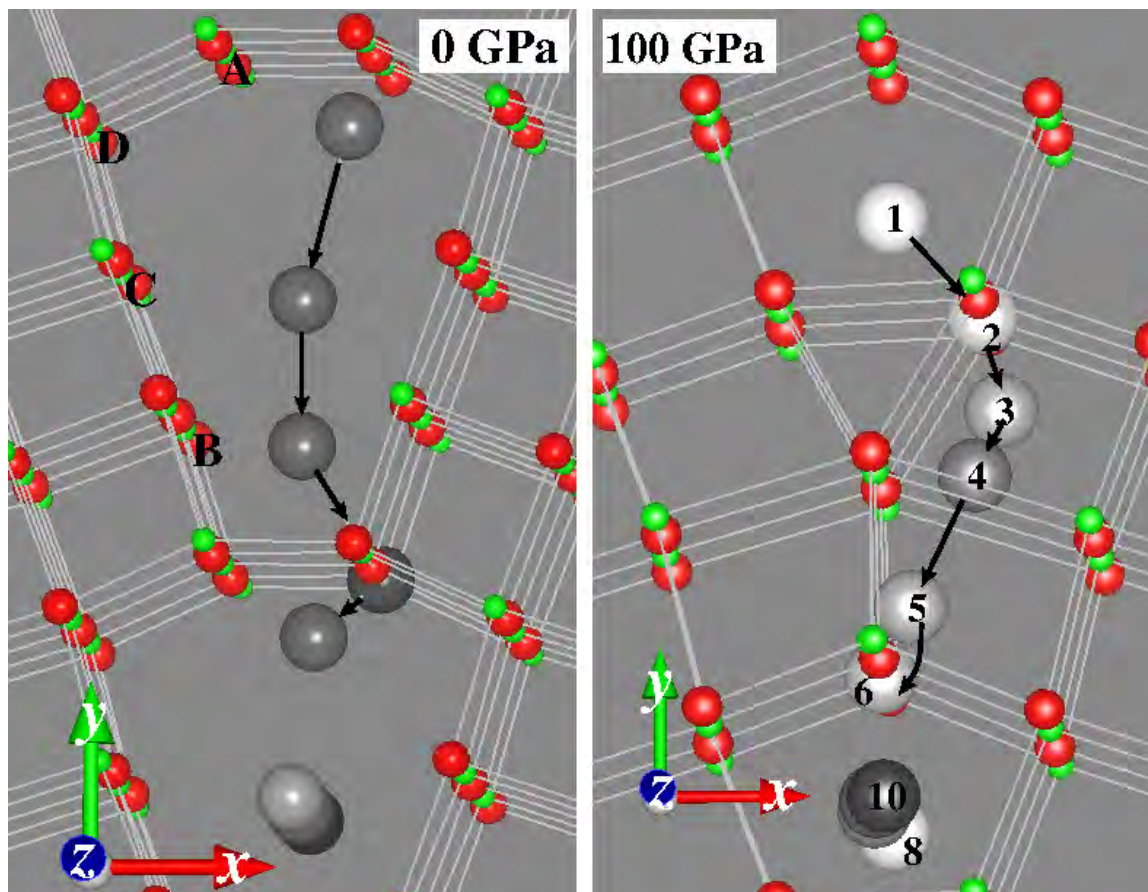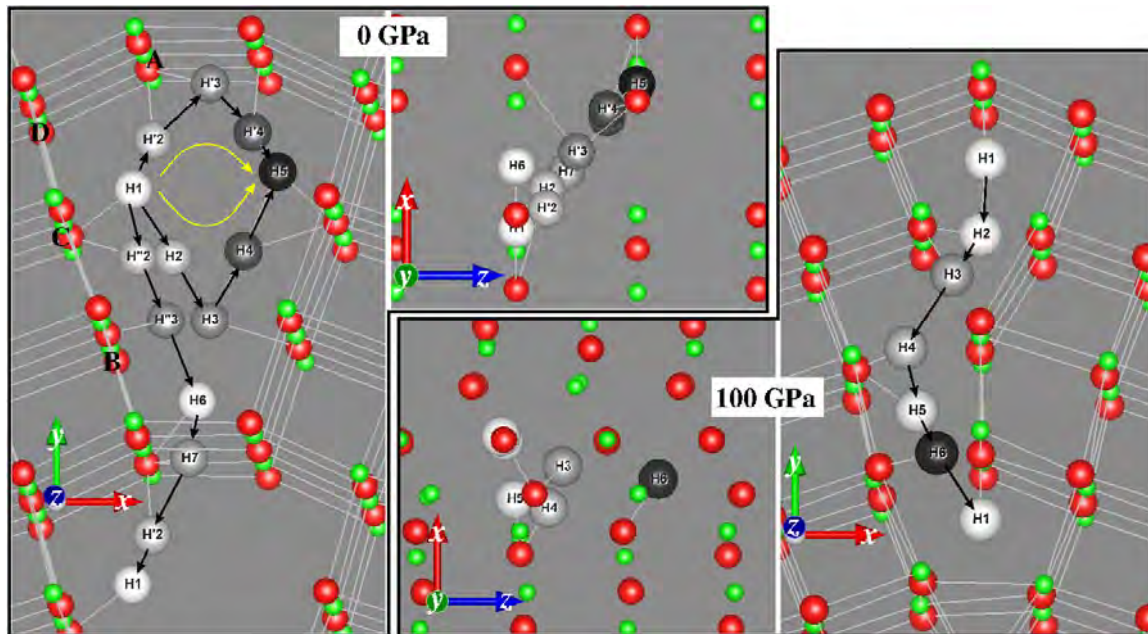


426

427

428

429

430

431

432

433

434

435

19

436

**FIGURE 4.** Predicted migration paths for interstitial proton at 0 and 100 GPa. Proton at its successive positions is shown by large sphere with grey-scale representing the *z*-coordinate. Some Mg-O bonds at GB are removed for the clarity. The green (small) and red (large) spheres represent Mg and O, respectively.

441

442



443

444

445
446

20